Nanoscale

PAPER

View Article Online
View Journal | View Issue

Cite this: *Nanoscale*, 2025, **17**, 25266

A fluorinated Janus-type dendrimer as an ionizable one-component nanocarrier for nucleic acids

Marta Rosati, [a] Nina Bono, [b] Lorenzo Fumagalli,[a] Federica Sebastiani,[c] Beatrice L. Bona,[a] Antonio Chaves-Sanjuan,[d] Najet Mahmoudi, [e] Giuseppina Raffaini,[f] Gabriella Cavallo, [a] Nicola Iacomino,[g] Claudia Malacarne,[g] Cristina Chirizzi,[a] Stefania Marcuzzo, [g,h] Giuseppe Lauria,[i,j] Gabriele Candiani, [b,h] Pierangelo Metrangolo *[a] and Francesca Baldelli Bombelli *[a]

Gene therapies based on nucleic acids (NAs) represent a new class of emerging drugs for the cure and prevention of several pathologies. NAs encounter significant challenges in intracellular uptake due to enzymatic degradation and their negative charge, which hinders membrane crossing. Specialized delivery carriers are used to allow NAs' cellular internalization and release in the cytosol for effective biological function. Among non-viral vectors, dendrimers have emerged as promising candidates, but the high costs of synthesizing high-generation dendrimers may limit their clinical use. Supramolecular dendrimers can be a compelling alternative. In this context, we developed a 2nd-generation Fluorinated Janus-type dendrimer (**FJD$_2$N**) accurately designed to feature a robust, ^{19}F-MRI-traceable hydrophobic self-assembling moiety, an optimal balance between fluorinated and hydrophilic groups, and an appropriate number of protonable primary amines. We showed that the designed dendrimer can effectively form dendriplexes with the NAs and safely transport them into different cell types, with successful transfection efficacies and low cytotoxic effects.

Received 29th July 2025,
Accepted 21st October 2025

DOI: 10.1039/d5nr03209a

rsc.li/nanoscale

Introduction

As an increasing number of genetic alterations are identified as causes of complex diseases, various gene therapies are becoming available for affected patients.[1] Due to their intrinsic low stability and high degradability, nucleic acids (NAs) need to be protected, reach the target cells, and fulfil their therapeutic functions.[2] Among non-viral approaches, lipid and polymer-based systems are the most studied carriers.[3–5] Also, dendrimers exhibit significant potential for NA delivery due to their chemical tunability, multivalent structure, and high payload capacity.[6–8] However, complex and costly production processes required for high-generation dendrimers have hindered their clinical translation, to date.[9]

More recently, amphiphilic dendrimers have been explored for NA delivery. This class of dendrimers, while possessing relatively simple molecular structures, self-assemble in aqueous solutions into supramolecular aggregates, *e.g.*, micelles, and combine the beneficial properties of both dendrimers and traditional delivery systems within a single nanostructure. Based on their structure, amphiphilic dendrimers can be classified as core–shell, Janus-type, and dendron-tail structures.[10] In particular, Janus-type dendrimers are composed of two different dendrons, each featuring distinct hydrophobic and hydrophilic components. The hydrophobic portions enable the dendrimer to self-assemble in aqueous environments, while the hydrophilic segments often contain

[a]*SupraBioNanoLab, Department of Chemistry, Materials, and Chemical Engineering "Giulio Natta", Politecnico di Milano, 20131 Milan, Italy.*
E-mail: pierangelo.metrangolo@polimi.it, francesca.baldelli@polimi.it
[b]*BioCell, Department of Chemistry, Materials, and Chemical Engineering "Giulio Natta", Politecnico di Milano, 20133 Milan, Italy*
[c]*Department of Pharmacy, Faculty of Health and Medical Sciences, University of Copenhagen, 2100 Copenhagen, Denmark*
[d]*Cryo-EM Lab, Department of Biosciences, University of Milan, 20131 Milan, Italy*
[e]*ISIS Neutron and Muon Spallation Source, STFC Rutherford Appleton Laboratory, Oxfordshire OX110QX, UK*
[f]*Department of Chemistry, Materials, and Chemical Engineering "Giulio Natta", Politecnico di Milano, 20133 Milano, Italy*
[g]*Neuroimmunolgy and Neuromuscular Diseases Unit, Fondazione IRCCS Istituto Neurologico Carlo Besta, 20133 Milan, Italy*
[h]*Brain-targeted Nanotechnologies (BraiNs) Lab, Fondazione IRCCS Istituto Neurologico Carlo Besta, Milan, Italy*
[i]*ALS Centre, 3rd Neurology Unit, Fondazione IRCCS Istituto Neurologico Carlo Besta, Milan, Italy*
[j]*Department of Medical Biotechnology and Translational Medicine, University of Milan, Milan, Italy*

ionic groups, guaranteeing the colloidal stability of the obtained assemblies. Amphiphilic dendrimers bearing protonable groups,[11–15] typically amines, can efficiently bind NAs.

In this context, our target was to design a structurally simple amphiphilic dendrimer possessing strong self-assembling capability, high transfection efficiency, and low cytotoxicity, by exploiting a branched fluorinated residue as hydrophobic entity. We recently reported that branched fluorinated moieties drive the self-assembly of highly fluorinated DNA amphiphiles, allowing for a tuneable stability for either short-term or long-term gene silencing applications.[16] However, to the best of our knowledge, there are no examples in the literature on the use of branched fluorinated moieties for the design of amphiphilic Janus-type dendrimeric nanocarriers for NA delivery. Peng *et al.* recently reported a dendron-tail structure bearing a terminal perfluorobutyl residue on the hydrophobic portion, which self-assembled into spherical micelles showing excellent stability and high loading encapsulation efficiency of an anticancer drug.[17] Inspired by these results, we targeted the first example of fluorinated Janus-type dendrimer for NA delivery.

Fluorinated dendrimers have already demonstrated high gene delivery efficacies and low cytotoxicity.[18,19] In particular, fluorination of NA vectors increases cellular uptake[20–22] and endosomal escape,[23–25] while providing the vector with ^{19}F-MRI traceability.[26,27] However, their structural design encompassed, almost exclusively, the functionalization of the surface amino groups of high-generation dendrimers, typically 5th, with perfluoroalkyl chains of various chain lengths.[16,28–31] Instead, we devised a low-generation polyester dendron conjugated to a branched polyfluoropentaerythrityl dendron bearing 27 magnetically equivalent ^{19}F atoms. On the one hand, the strong self-assembling tendency of the branched fluorinated dendron[32–35] was expected to facilitate the efficient formation of nano-assemblies in aqueous solution, as a consequence of the fluorophobic effect.[19,36] On the other hand, functionalizing the hydrophilic part with primary amino groups, *i.e.*, $-NH_2$, would provide the dendron with protonable recognition sites for NA binding *via* charge-assisted hydrogen bonding (HB).

Furthermore, fluorinated dendrimer-based vectors for NAs have mostly relied on polyamidoamine (PAMAM),[37–40] poly(propylenimine) (PPI),[41] and poly-L-lysine (PL) scaffolds.[42,43] Instead, we selected a bis-MPA (or 2,2-bis(hydroxymethyl)propionic acid) dendron, for the first time, for its biodegradability and low cytotoxicity, which renders it well suited for use in biological applications.[44] Recently, we reported the synthesis of a new family of low-generation non-ionic Fluorinated bis-MPA Janus-type Dendrimers (generations 1–3, FJD_{1-3}),[45] which showed excellent self-assembly features in aqueous solutions, as a function of the balance between their hydrophobic and hydrophilic moieties. To develop an efficient NA nanocarrier, we selected the 2nd-generation FJD_2 for its optimal balance between fluorinated and hydrophilic parts, which is crucial for improving transfection efficiencies.[46]

Hence, in this work we report the chemical modification of FJD_2 with four primary amino groups to obtain an ionizable 2nd-generation Fluorinated Janus Dendrimer (Fig. 1a), **FJD_2N**. We demonstrate that the obtained dendrimer is highly dispersible in aqueous media as a single component and forms micelles, which strongly interact with NAs forming ^{19}F-MRI visible supramolecular dendriplexes (complexes between dendrimers and NAs), which were fully characterized in terms of their structure and colloidal stability (Fig. 1b). In addition, **FJD_2N** showed a significant ability to transfect nucleic acids in various cell lines at safe concentrations, confirming the potential of the developed dendrimer as a ^{19}F-MRI-traceable gene delivery vector.

Results and discussion

Molecular design of the protonable Janus-type fluorinated dendrimer

The molecular structure of **FJD_2N** (Fig. 1a) was carefully designed to obtain high NA complexation and low cytotoxicity (mostly related to the density of positive charges and selected chemical skeleton). To this aim, the biodegradable dendron bis-MPA[44,47] was chosen as an alternative to more conventional dendrimeric carriers, such as PAMAM, PPI, and PL.

Primary ammonium headgroups were, instead, selected as NA binding sites acting *via* a twofold recognition mechanism, *i.e.*, ion-pairing and charge-assisted HB with the NA phosphate groups.[14,48,49] The 2nd-generation derivative was chosen based on our previous results on the self-assembly of non-ionic **FJD_{1-3}**,[45] in which **FJD_2** showed the highest dispersibility and colloidal stability. Furthermore, the low-generation guarantees a limited number of positive charges, thus, possibly reducing cytotoxic effects.

Molecular Dynamics (MD) simulations (Fig. S1 and Table S1 in SI) showed that **FJD_2N** is characterized by hydrophobic (650 Å^3) and hydrophilic (681 Å^3) moieties of comparable molecular volumes, an optimal feature for dendrimers' transfection efficiencies.[13] Furthermore, the structural molecular parameters obtained by MD were useful in determining the molecular packing parameter (p.p. = 0.09) of **FJD_2N**, which suggests the potential formation of spherical micelles in aqueous media[50] (Table S1 in SI). The synthetic procedure adopted for **FJD_2N** has been based on the published protocol,[45] which has been extended with the insertion of primary ammonium residues by deprotecting the Boc groups of the condensed 3-[(2-methylpropan-2-yl)oxycarbonylamino]propanoic acid (see Schemes S1 and S2, in SI).

The pK_a of **FJD_2N**, measured by potentiometric titration[51] (Fig. S2 and Table S2 in SI), resulted equal to 9.4 which suggests that, at physiological pH, it should have almost 99% of the amines still protonated. The anion-coordination ability of **FJD_2N** was demonstrated by ^{1}H-NMR titration experiments in deuterated DMSO[48] (Fig. S3, S4 and Tables S3, S4 in SI). We extrapolated an association constant (K_{ass} = 30 M^{-1}) for chloride ions, which is in line with the K_{ass} observed for dendrimers of the same generation exposing primary amines.[52] Furthermore, we studied the interactions between **FJD_2N** and a

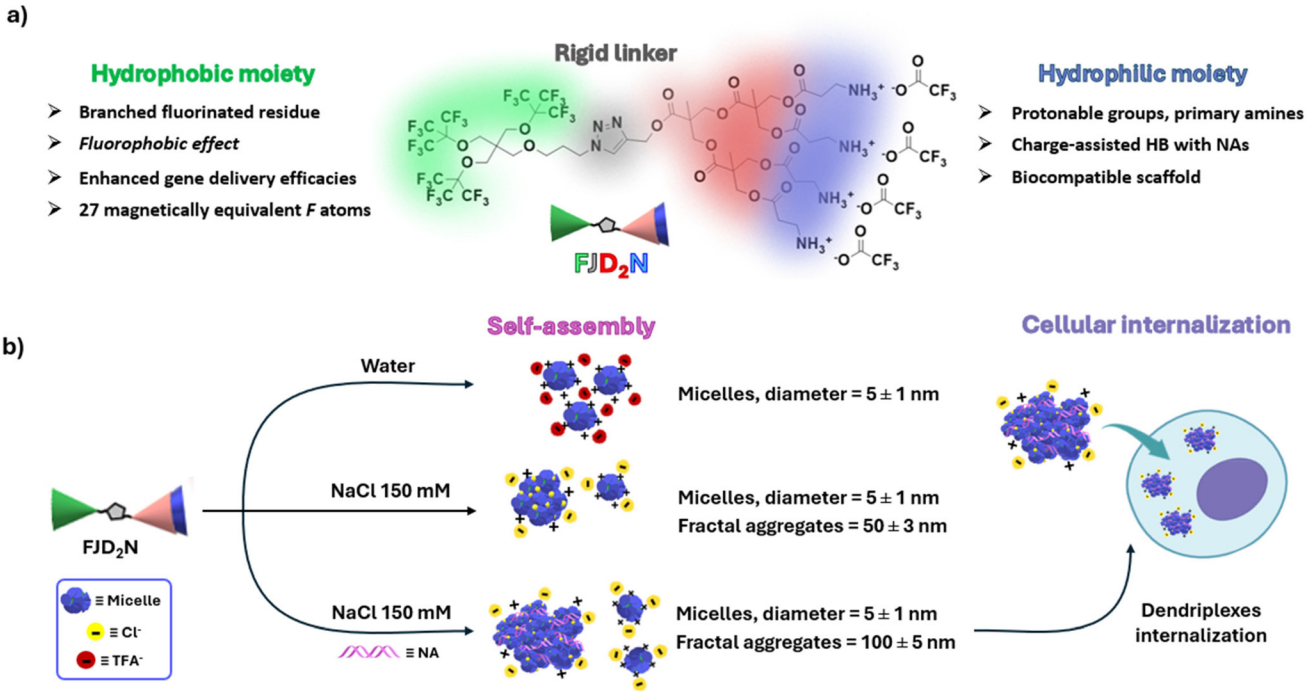

Fig. 1 (a) Design and structure. The 2nd-generation Fluorinated Janus Dendrimer (**FJD$_2$N**) exploits a branched fluorinated moiety as hydrophobic part working as strong self-assembling moiety. The hydrophilic part was selected to combine a biocompatible and biodegradable scaffold with a minimal number of primary ammonium groups to allow NA binding through charge assisted Hydrogen Bonding (HB), while minimizing the density of positive charges, and thus limiting cytotoxic effects. (b) Self-assembly in aqueous solutions and NA internalization into cells. The dendrimer is directly dispersible in water where it self-assembles forming positively charged micelles, which, in presence of ions, tend to aggregate forming larger fractal aggregates composed by small **FJD$_2$N** micelles, held together by charge-assisted hydrogen bonding and electrostatic interactions. Dimensions of fractal aggregates are taken from Cryo-TEM images. **FJD$_2$N** is able to deliver plasmids and RNA into different cell lines, thus efficiently working as a gene delivery vector.

Cy5-modified Luciferase GL3 siRNA by fluorescence titration experiments, by adding increasing amounts of **FJD$_2$N** to a constant concentration of the NA (0.6 μM, see Table S5 and Fig. S5 in SI).[53] As highlighted in Fig. 2a, we observed a progressive quenching of the fluorescence, reaching 90% reduction compared to the intensity of the free RNA. The largest fluorescence decrease was observed at N/P ratios (where N is the number of nitrogen groups and P the number of phosphates) close to 2, suggesting that 2 ammonium groups are required to efficiently bind each phosphate group of RNA in a 2 : 1 host–guest ratio (Fig. 2b). By fitting the data with a 2 : 1 model, we were able to extrapolate an association constant on the order of 10^9 M^{-2} (see Table S6 in SI), which demonstrates the excellent anion binding capability of **FJD$_2$N** compared to similar systems.[54] We assign the observed fluorescence quenching to an energy transfer likely occurring between Cy5-modified Luciferase GL3 siRNA molecules in close spatial proximity as a consequence of their interactions with **FJD$_2$N**, as already reported elsewhere for similar cyanine dye-modified NAs.[55]

Finally, we also evaluated the ability of **FJD$_2$N** to complex NAs by monitoring the fluorescence emission of SYBR® green fluorescent probe using salmon sperm DNA and Luciferase GL3 siRNA at different N/P ratios. Similarly, full NA complexation was reached at N/P values of 2.5 for DNA and 2 for siRNA (Fig. 2c and d), respectively. These results are in line with titration results and with N/P values already reported for similar non-fluorinated bis-MPA-based low-generation amphiphilic dendrons.[11] Altogether, these findings demonstrate the strong anion binding capability of **FJD$_2$N** at very low N/P ratios,[28] which is highly instrumental for its exploitation as NA vector.

FJD$_2$N self-assembling properties in aqueous solutions

Positively-charged micelles are optimal nanocarriers for the delivery of NAs to cells.[56] **FJD$_2$N** can be directly dispersed in aqueous solutions without addition of cosolvents and/or surfactants. When dispersed, it aggregates at a critical micellar concentration (CMC) of 67 μM and 20 μM, in pure water and NaCl 150 mM, respectively, as determined by monitoring the pyrene fluorescence emission as a function of the **FJD$_2$N** concentration (Fig. S6, S7 and Tables S7–S9 in SI).[57] **FJD$_2$N** assemblies in water resulted positively charged with zeta-potential values of about +50 mV (Table S10 in SI). The colloidal stability and hydrodynamic size of **FJD$_2$N** self-assemblies were then studied over time at two different concentrations well-above the CMC (2.5 mM and 0.5 mM) by Dynamic Light Scattering (DLS).

FJD$_2$N self-assembly in pure water did not seem strongly dependent on concentration, as highlighted by the superimpo-

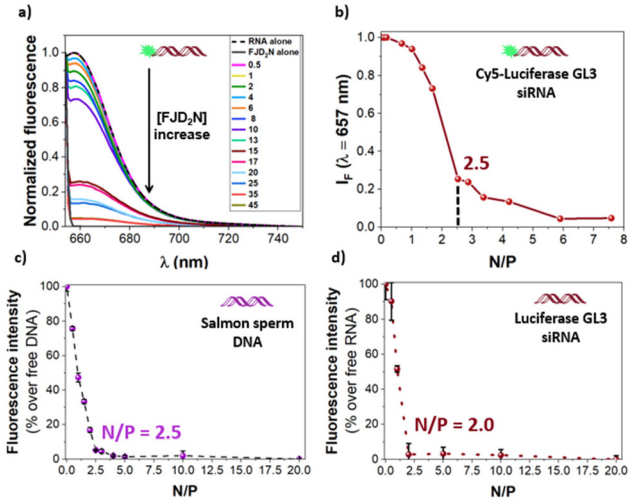

Fig. 2 **FJD_2N**-NA coordination. (a) Fluorescence spectra (λ_{ex} = 651 nm; λ_{em} = 654–750 nm) of Cy5-modified Luciferase GL3 siRNA (0.6 μM) at increasing amount of **FJD_2N** (from 0.5 μM to 45 μM). The fluorescence spectrum of the pure **FJD_2N** (2.9 mM) is also shown in dark grey. (b) Variation of the normalized fluorescence intensity at increasing N/P ratios. (c) Normalized fluorescence intensity for increasing amounts of **FJD_2N** in solutions containing a constant concentration of salmon sperm DNA in 10 mM HEPES (pH = 7.4). (d) Normalized fluorescence intensity for increasing amounts of **FJD_2N** in solutions containing a constant concentration of Luciferase GL3 siRNA in NaCl 150 mM.

sition of the auto-correlation functions reported in Fig. 3a at different **FJD_2N** concentrations.[58] The DLS autocorrelation functions appeared invariant over 48 hours from dispersions preparation at RT for both concentrations (Fig. S8a and b in SI). The cumulant analysis of the auto-correlation functions showed a high polydispersity of the assemblies with PDI values of around 0.3–0.4 (Table S10 in SI), as confirmed by the presence of two different populations in the intensity-weighted size distributions obtained by CONTIN analysis (Fig. S8c in SI). However, the CONTIN number-weighted analysis (Fig. 3b) indicated that the most abundant population was composed by small micelles of around 2 ± 0.2 nm of hydrodynamic radius.

To further characterize the structure of **FJD_2N** assemblies in aqueous solution, we performed Small Angle X-ray and Neutron Scattering (SAXS and SANS) analyses. **FJD_2N** dispersions were measured at both 0.5 mM and 2.5 mM, and resulting curves showed no dependence on concentration, in agreement with DLS findings. For SANS experiments, **FJD_2N** dispersions were prepared in solvents with five different D_2O contents, to take advantage of the contrast variation, which allows to determine assembly features that go beyond size and shape.

SANS (Fig. 3c and S9 in SI) and SAXS curves (Fig. S10 in SI) were comparable and simultaneously fitted with a linear combination of sphere and fractal models.[59–61] The combined model indicated the coexistence of spherical micelles and fractal aggregates with the micelles as building blocks. The micelles had a diameter of 5 ± 1 nm, while the fractal aggregates had a correlation length on the order of 100 ± 5 nm (Tables S11–S13). In pure water, free micelles account for 96% of **FJD_2N** assemblies in agreement with DLS results. Finally, in order to assess the effect of **FJD_2N** self-assembly on the magnetic properties of fluorine atoms in the micelles, we performed ^{19}F-NMR analyses at the two tested concentrations (0.5 mM and 2.5 mM). Besides the peak of the TFA counterions, the spectra revealed the presence of a broad single peak for [**FJD_2N**] = 2.5 mM (δ = −71.29 ppm, Fig. 3d), while decreasing the concentration to [**FJD_2N**] = 0.5 mM, two distinct peaks were observed (δ = −71.37 ppm, broad, and δ = −70.36, sharp, Fig. 3e). We ascribe the downfield-most signal to the dendrimer in aggregated form in solution, in slow exchange rate on the NMR time-scale with its monomeric form.[62]

Importantly, measurement of ^{19}F-NMR spectra overtime (Fig. S8d and e in SI) confirmed the dispersion stability, since no changes could be observed over 48 h for both tested concentrations. Furthermore, ^{19}F-NMR relaxivity parameters, T_1 and T_2, were determined at [**FJD_2N**] = 2.5 mM, which resulted 465 ms and 85 ms, respectively (Fig. S11 in SI).[63] The obtained values are in line with relaxivity parameters observed for the best ^{19}F-MRI probes.[64]

Dendriplexes characterization and phantom ^{19}F-MRI experiments

Transfection efficiency and cytotoxicity are known to strictly depend on the structures of the formed assemblies. Thus, we performed an in-depth study of the structure of the **FJD_2N**-Luciferase GL3 siRNA dendriplexes at three N/P ratios (*i.e.*, 20, 30, and 40) in NaCl 150 mM, mimicking physiological conditions, by combining DLS, Cryo-TEM, SAXS, SANS, and ^{19}F-NMR experiments.[65]

In comparison to dendrimer's dispersions in the same conditions, siRNA addition, for all investigated N/P ratios, induced slight changes in the auto-correlation functions (Fig. S12a–c in SI). In fact, in the presence of siRNA, a size increase of the smaller population and a size decrease of the larger aggregates (black arrows, Fig. 4a) were observed, with a consistent reduction of the PDI from cumulant fitting (Tables S14–S16 in SI). Zeta-potential experiments of the siRNA-loaded samples at the different N/P values were comparable and still showed very positive values (Z = +29–44 mV, Tables S14–S16 in SI).

SAXS and SANS measurements enabled us to get more insights into the supramolecular organization of the formed aggregates.

Both curves (Fig. 4b, c and Fig. S13, S14 in SI) for **FJD_2N** in NaCl presented no major differences from the curves collected in pure water, and hence the same combined model was used to analyze the data. Data analysis revealed that, in comparison to the dendrimer in pure water, by increasing the ionic strength, the population of small micelles decreased by 5 to 10% with a corresponding increase of the fractal aggregates (Fig. S13 in SI). This was also confirmed by Cryo-TEM experiments on the same samples that showed the formation of pseudo-spherical assemblies of 50 ± 3 nm for pure **FJD_2N**, while the samples complexed with siRNA were characterized

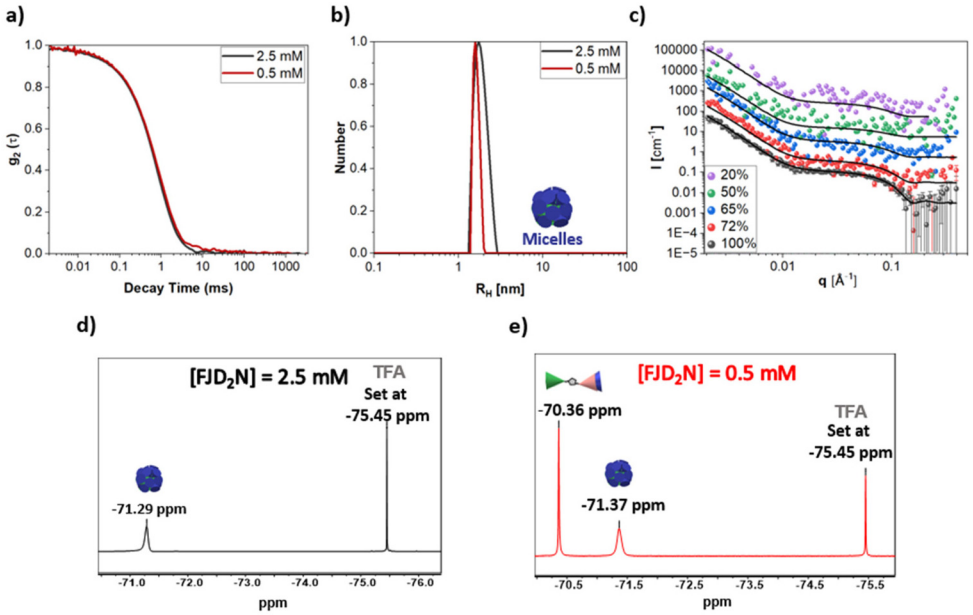

Fig. 3 **FJD$_2$N** self-assembly in water. (a) The good overlap between DLS auto-correlation functions of freshly prepared 2.5 mM and 0.5 mM **FJD$_2$N** dispersions suggests that the overall size of the aggregates is not affected by **FJD$_2$N** concentration (θ = 90°, RT). Color code: 2.5 mM = black, 0.5 mM = red. (b) Number-weighted hydrodynamic radius distribution obtained by CONTIN fitting of DLS auto-correlation function of 2.5 and 0.5 mM **FJD$_2$N** dispersions (freshly prepared, θ = 90°, RT) Color code: 2.5 mM = black, 0.5 mM = red. (c) SANS curves collected with **FJD$_2$N** 2.5 mM in five solvent contrasts (D_2O content reported as % in the legend) were fitted simultaneously with the combined model shown as black lines. The data and model were offset for clarity: 72% D_2O content by 10, 65% D_2O content by 100, 50% D_2O content by 1000, and 20% D_2O content by 10 000. (d) ^{19}F-NMR spectrum of freshly prepared **FJD$_2$N** aqueous solution at 2.5 mM. The peak set at −75.45 ppm is referred to the trifluoroacetate (TFA) counter ions, while the peak at −71.29 ppm is related to aggregated **FJD$_2$N**. Solvent: **FJD$_2$N** solution + D_2O (10 : 1 v/v). (e) ^{19}F-NMR spectrum of freshly prepared **FJD$_2$N** aqueous solution at 0.5 mM. Besides the peak of TFA (set at −75.45 ppm), two other peaks can be observed at −71.37 ppm related to the **FJD$_2$N** in the aggregate and −70.36 ppm related to **FJD$_2$N** monomeric form. Solvent: **FJD$_2$N** solution + D_2O (10 : 1 v/v).

by an additional dominant population of assemblies with sizes between 100 ± 5 nm (Fig. 4d and S12d).

Furthermore, the ^{19}F-NMR spectra of 0.56 mM **FJD$_2$N** dispersions in NaCl 150 mM with and without siRNA overlap, but they are different from that in pure water (Fig. 4e and S12e, f). The peak relative to **FJD$_2$N** monomeric form is not observable, suggesting an increased tendency of **FJD$_2$N** to self-assemble in the presence of salts, in accordance with the CMC reduction observed in these conditions. Interestingly, two broad peaks were observed at around −71.5 ppm, consistent with at least two different environments for the F atoms in the dendriplexes.

Relaxivity parameters for the two peaks were similar and close to the ones measured in pure water (T_1 = 440 ms, T_2 = 89 ms, Fig. S15 in SI), suggesting that the fluorinated chains remain quite mobile in the supramolecular assemblies. A further demonstration of this was given by preliminary phantom studies on a 7T scanner (using a dual-transmit receive ^{19}F/^{1}H volume coil) integrated with an ultra-shielded horizontal bore magnet on **FJD$_2$N** samples in water, NaCl 150 mM, and after complexation with siRNA (N/P = 30). As shown in Fig. 4f and S16 in SI, **FJD$_2$N** gave a bright and comparable ^{19}F-MRI signal in all tested conditions at the highest concentration.

All data indicate that **FJD$_2$N** self-assembles almost exclusively into 5 nm-micelles in pure water. Instead, in presence of Cl^- anions, micelles are glued together in larger aggregates as a result of anion coordination by electrostatic pairing and hydrogen bonding. In the presence of NAs, fractal aggregates of the micelles are obtained as a consequence of the multivalent binding between the $-NH_3^+$ groups of **FJD$_2$N** and the NA phosphates *via* charge-assisted hydrogen bonding.

Cytotoxicity and transfection efficacy on different cells lines

It has been reported that dendriplexes of sizes close to 100 nm can be easily internalized into cells.[66] Therefore, we next studied **FJD$_2$N** ability to deliver NAs into the cytosol. We performed a systematic *in vitro* transfection study using **FJD$_2$N** and the plasmid pGLuc-Basic 2, a reporter vector encoding secreted Gaussia luciferase.

Various N/P ratios were used to evaluate both transfection efficacy and cytotoxicity onto three different cell lines: L929 murine fibroblasts from subcutaneous connective tissue, SH-5YSY human neuroblastoma cell line, and C2C12 cells, an immortalized mouse myoblast cell line. JetPEI®[67] and Lipofectamine™ 3000, polymeric and lipidic commercially available gene delivery vectors, respectively,[68] were used as controls. As highlighted in Fig. 5a–c and S17 in SI, cell viability resulted dependent on cells type, showing lower cytotoxic levels than selected commercial benchmarks up to N/P = 40 (equal to a final [**FJD$_2$N**] = 30 μM) for L929 and SH-5YSY, while

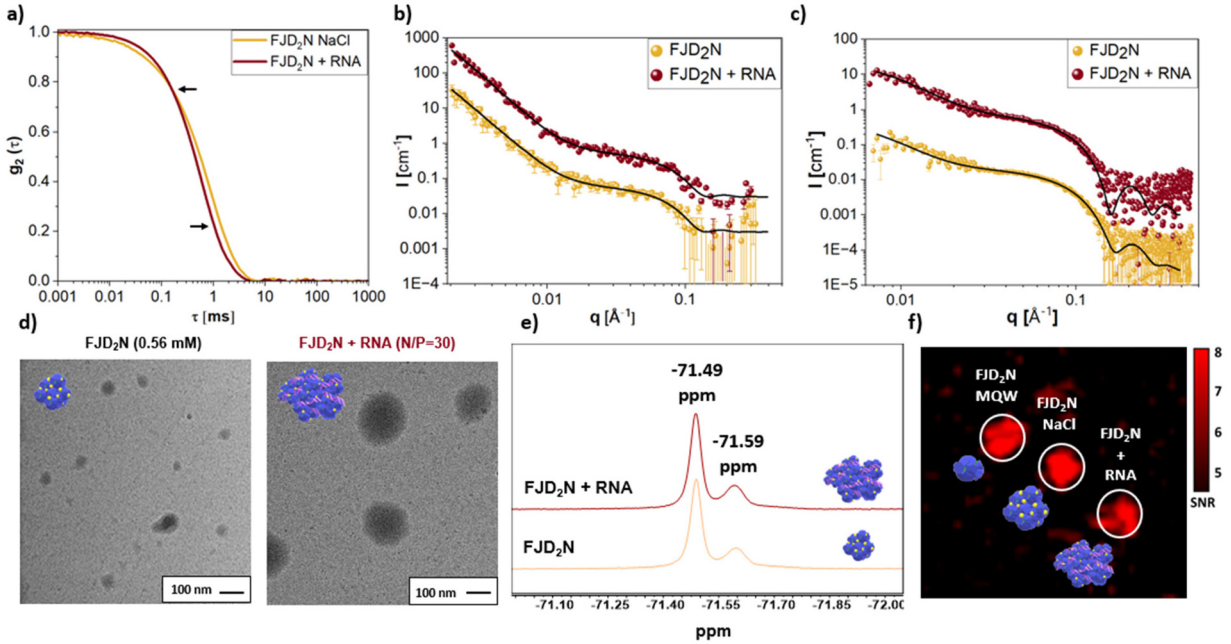

Fig. 4 Dendriplexes characterization in comparison with **FJD$_2$N** self-assembly in NaCl 150 mM. (a) Overlay of the DLS auto-correlation functions between fresh 0.56 mM **FJD$_2$N** dispersions in NaCl 150 mM and dendriplexes' dispersions at N/P = 30 (θ = 90°) at the same **FJD$_2$N** concentrations with Luciferase GL3 as siRNA. Colour code: **FJD$_2$N** = yellow; dendriplexes at N/P 30 = red. (b) Overlay of SANS curves collected with dendriplexes, made of **FJD$_2$N** 0.56 mM and siRNA Luciferase GL3 (N/P = 30), and **FJD$_2$N** 0.56 mM (freshly prepared) at the same contrast (D_2O content 100%). The data and model were offset for clarity, fitting curve is shown as a continuous line. Colour code: **FJD$_2$N** = yellow; dendriplexes at N/P 30 = red. (c) Overlay of SAXS curves collected with dendriplexes made of **FJD$_2$N** 0.56 mM and Luciferase GL3 (N/P = 30) and **FJD$_2$N** 0.56 mM (freshly prepared). Data were collected at two time points, and they were fitted to the combined model shown as a continuous line. The data and model were offset for clarity. Colour code: **FJD$_2$N** = yellow; dendriplexes at N/P 30 = red. (d) Cryo-TEM images of **FJD$_2$N** 0.56 mM and dendriplexes at N/P = 30. Scale bar: 100 nm. (e) Comparison between ^{19}F-NMR spectra of freshly prepared dispersions of 0.56 mM **FJD$_2$N** in NaCl 150 mM and dendriplexes' dispersions at the same **FJD$_2$N** concentrations with Luciferase GL3 as siRNA (N/P = 30). Colour code: **FJD$_2$N** = yellow; dendriplexes at N/P 30 = red. Solvent: **FJD$_2$N** solution + D_2O (10 : 1 v/v). (f) ^{19}F-MRI phantom images of **FJD$_2$N** solution 2.5 mM in pure water, in NaCl 150 mM, and in presence of Luciferase GL3 as siRNA at N/P = 30.

higher sensitivity to **FJD$_2$N** was observed for the C2C12 cells with acceptable cytotoxicity up to N/P = 30 (equal to a final [**FJD$_2$N**] = 23 μM). Transfection efficiencies are expressed as luminescence signal (in relative light units, RLU). For all tested cell lines, RLU levels are comparable with those observed for JetPEI® and Lipofectamine™ 3000. Overall, this study shows that **FJD$_2$N** can successfully transfect all tested cells with good viability up to 23 μM, which corresponds to N/P ratio of 30 (Table S17 in SI). Additionally, to better assess the viability of **FJD$_2$N**, we performed further studies on a primary cell line, such as ependymal stem progenitor cells (epSPCs), which demonstrated much higher viability at all tested N/P ratios, compared to lipofectamine (Fig. S18 in SI).

Finally, to further confirm the internalization of the NA in transfected cells, we performed confocal microscopy on C2C12 cells treated with Cy5-conjugated Luciferase GL3 siRNA complexed with **FJD$_2$N** at N/P ratio = 30 (see Tables S18, S19 and Fig. S19 in SI) at 24, 48, and 72 h following administration. As shown in Fig. 6, Cy5-modified Luciferase GL3 siRNA (indicated by red spots) was significantly internalized by the cells within 24 h of treatment, demonstrating colocalization with the Desmin-stained cytoplasm (marked in green). After 48 h, these red spots remained detectable in the cytoplasm, and side views from the *z*-stack images further revealed that some colocalized with the DAPI-stained nuclei (shown in blue). However, after 72 h of incubation, a decrease in the fluorescence of the red spots was observed, which may be attributed to cellular proliferation and RNA processing. These findings confirm that **FJD$_2$N** facilitate NA internalization into cells and NA cargo release.

Experimental

Molecular design of the protonable Janus-type fluorinated dendrimer

General information. For the synthesis, the employed chemicals as reactants and solvents were used as received without further purification and purchased with purity >97% from: ©TCI Deutschland GmbH; Sigma Aldrich; Fluorochem. Thin layer chromatography TLC was conducted on plates precoated with silica gel Si 60-F254 (Merck, Darmstadt, Germany). Flash chromatography was carried out on J. T. Baker silica gel mesh size 230–400.

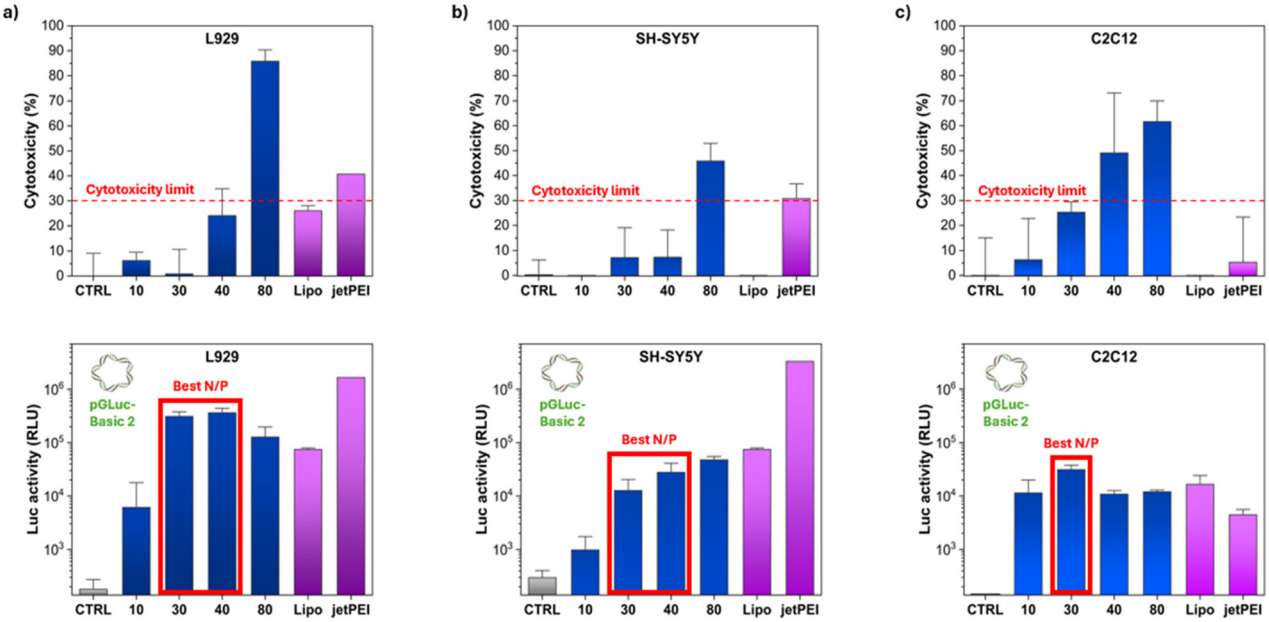

Fig. 5 Cytotoxicity (up) and transfections results (down) on (a) L929 murine fibroblasts from subcutaneous connective tissue, (b) SH-5YSY human neuroblastoma cell line, and (c) C2C12, immortalized mouse myoblast cell line using the plasmid pGLuc-Basic 2-**FJD$_2$N** dendriplexes at different N/P ratios. Results are compared with complexes of commercial benchmarks JetPEI® and Lipofectamine™ 3000 with the same pDNA. Red dotted lines indicate cytotoxicity accepted limits, while red rectangles highlight best **FJD$_2$N** to NA N/P ratios considering transfection efficiency and cytotoxicity.

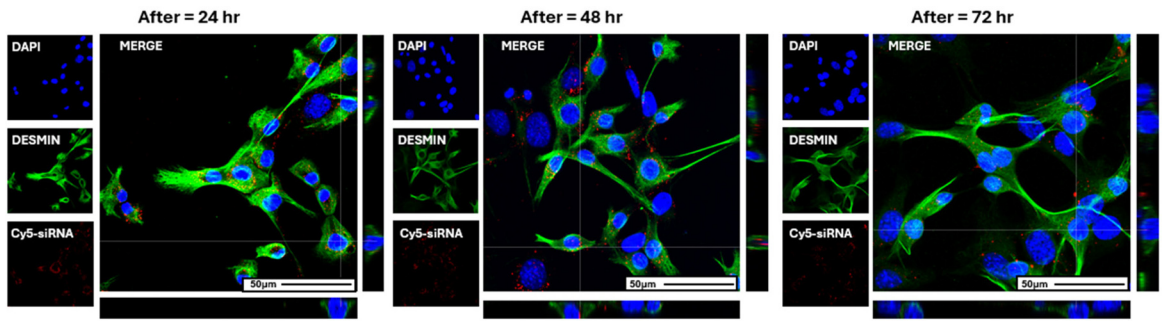

Fig. 6 Intracellular localization of **FJD$_2$N**/siRNA dendriplexes (N/P = 30) in C2C12 cells observed with confocal laser scanning microscopy after 24, 48, and 72 h of incubation. Desmin was used to stain cytoplasm (in green), DAPI was used to stain nuclei (in blue), and Luciferase GL3 siRNA was labelled with Cy5 (in red); scale bar = 50 μm. For each time point, details of the three channels used are reported next to the merged image. Side view of the orthogonal *z*-stack (view: in the *x* and *z* plane and in the *y* and *z* plane) are reported for each merged image.

All the NMR spectra were recorded on a Bruker AV400 Bruker AvanceII 400 MHz spectrometer equipped with a 5 mm QNP probe (^{19}F, ^{31}P–^{13}C/^{1}H). NMR spectra were recorded at (300 ± 3 K) and chemical shifts are reported in ppm downfield from SiMe4 with the residual proton ($CDCl_3$ d = 7.26 ppm, CD_3OD: d = 3.31 ppm) and carbon ($CDCl_3$: d = 77.0 ppm, CD_3OD: d = 49.0 ppm). Proton and carbon assignments were achieved by means of ^{13}C-NMR, ^{1}H–^{1}HCOSY, and ^{1}H–^{13}C-HSQC experiments. Coupling constant values, J, are given in Hz. Data evaluation was done with MestreNova 10.0 from Mestre-Lab. The samples prepared for the characterization of the compound synthesized were prepared by dissolving 5–10 mg in 500 μL of deuterated solvent. Methanol-d4 (99 atom % D), deuterated water (D_2O, 99 atom % D), dimethyl sulfoxide (DMSO, 99 atom % D), and chloroform-d, 99.8 atom % D were purchased from Sigma Aldrich, Germany.

FTIR was measured with a Thermo Scientific Nicolet iS50 FTIR spectrometer, equipped with iS50 ATR accessory (Thermo Scientific, Madison, USA). IR signal values were expressed in wavenumber (cm^{-1}) and rounded to the nearest whole number through automatically assignment using OMNICTM IR software. Air was recorded as background. The analysis was made in transmittance mode in a wavenumber window of 4000–400 cm^{-1}. High resolution ESI Mass spectrometry was done by UNITECH COSPECT: Comprehensive Substances characterization *via* advanced spectroscopy Via C. Golgi 19, University of Milan. Inductively Coupled Plasma Optical Emission spectroscopy (ICP-OES) analyses were performed in

the *Laboratorio di Analisi chimiche* of Politecnico di Milano, Via Luigi Mancinelli 7, Milan. The value is reported as an average of four measurements on four different synthetic batches.

Molecular mechanics and molecular dynamics simulations. The theoretical study is based on Molecular Mechanics (MM) and Molecular Dynamics (MD) simulations. All MM and MD simulations were performed with Materials Studio, Discovery Studio packages (version 7.0, BIOVIA, Accelrys Inc., San Diego, CA, USA). Using the same simulation protocol proposed in previous work,[69] all calculations are performed with CVFF force field with a Morse potential for the bonded atoms, in water (1120 water molecules), considering periodic boundary conditions of the system in a cubic cell of size 33.0 Å. The simulation protocol involved three sequential steps: (i) at first the initial energy minimization; (ii) the MD run in an NVT ensemble at constant temperature; (iii) the final geometry optimization of the configuration assumed by the system at the end of MD run when the equilibrium state was achieved. All energy minimizations were carried out using the Conjugate Gradient algorithm up to an energy gradient lower than 4×10^{-3} kJ mol^{-1} Å^{-1}.

The MD simulation lasting for 2 ns was performed at a constant temperature (300 K), controlled through the Berendsen thermostat. Integration of the dynamical equations was carried out with the Verlet algorithm using a time step of 1 fs, and the instantaneous coordinates were periodically saved every 2 ps for further analysis.

The packing parameter has been obtained by using the formula:

$$\text{packing parameter} = \frac{v}{(a_0 \cdot l_d)}.$$

The total volume of the minimized molecule of each amphiphile (v) has been divided for the product obtained by multiplying the solvent accessible area occupied by the hydroxyl groups (a_0) of each amphiphile and the maximum extended length of the amphiphile (l_d).

From literature, molecules showing a packing parameter <0.33 tend to form micelles.[50]

Synthesis of FJD$_2$N. Compounds **1** to **3**, **DG$_1$**, **DG$_2$**, and **F$_{27}$-N$_3$** were prepared according to procedures previously reported in literature.[45] Full synthetic steps are reported in Schemes S1 and S2, in SI.

FJD$_1$. Compound **DG$_1$** (13.7 mg; 0.08 mmol) and copper(I) acetate (1 mg; 0.008 mmol) were transferred into a round-bottom flask and solubilized in 1 mL of THF. Separately, compound F_{27}-N_3 (62 mg; 0.07 mmol) was solubilized in 1 mL of THF and added to the flask. The reaction was run overnight, at 55 °C, under magnetic stirring and N_2 flux. To verify that the reaction had occurred, a Thin Layer Chromatography (TLC) was performed employing hexane/ethyl-acetate (8 : 2) as eluent. Subsequently, to purify the reaction product from copper residues, an extraction with a solution 0.1% m/v of disodium EDTA in water and dichloromethane was performed. The organic phase was then dried on Na_2SO_4 and then dried by means of rotary evaporator. The product was obtained as an uncolored oil (yield: 80%). ^{1}H NMR (400 MHz, methanol-d_4) δ 7.96 (s, 1H), 5.23 (s, 2H), 4.46 (t, J = 7.1 Hz, 2H), 4.16 (s, 7H), 3.77–3.53 (m, 4H), 3.47 (t, J = 6.1 Hz, 2H), 3.44 (s, 2H), 2.17 (p, J = 6.6 Hz, 2H), 1.15 (s, 3H). ^{13}C NMR (101 MHz, methanol-d_4) δ 176.23, 144.36, 125.72 (d, J = 50.4 Hz), 123.28–117.10 (m), 81.53–80.16 (m), 69.17, 67.16, 67.11, 65.86, 58.44, 51.70, 48.40, 47.50, 31.29, 17.22. ^{13}C NMR (101 MHz, methanol-d_4) δ 176.23, 144.36, 125.47, 126.28–117.17 (q, $^1J_{C-F}$ = 291.8 Hz), 81.83–80.16 (m), 69.17, 67.16, 67.11, 65.86, 58.44, 51.70, 48.40, 47.50, 31.29, 17.22. ^{19}F NMR (376 MHz, MeOD) δ −71.51. ATR-FTIR: stretching O–H: 3650–3000 cm^{-1}; stretching C–H: 2970–2800 cm^{-1}; stretching C=O: 1726 cm^{-1}; stretching C–F: 1300 cm^{-1}; bending C–F: 700 cm^{-1}.

FJD$_2$. Compound **DG$_2$** (113.5 mg; 0.28 mmol) and copper(I) acetate (3.8 mg; 0.03 mmol) were dissolved in 1 mL of THF under inert atmosphere. Separately, **F$_{27}$-N$_3$** (244 mg; 0.28 mmol) was dissolved in other 2 mL of THF and transferred to the reaction mixture. The reaction was run under stirring and nitrogen atmosphere at 55 °C overnight. The formation of the product was confirmed by analyzing at FTIR 100 µL of the solution by monitoring the disappearance of the characteristic stretching of the azido group (2100 cm^{-1}). The reaction was stopped, added to iced water and extracted with CH_2Cl_2; then, the organic phase was washed two times with a 0.1% m/v disodium EDTA solution and with a saturated NaCl solution in water. The organic phase was collected, dried with Na_2SO_4, and rotary evaporated. The compound was collected as a sticky solid (yield: 80%). ^{1}H NMR (400 MHz, methanol-d_4) δ = 8.08 (s, 1H), 5.31 (s, 2H), 4.53 (t, J = 7.2, 2H), 4.40–4.27 (m, 4H), 4.22 (s, 6H), 3.74–3.59 (m, 8H), 3.54 (t, J = 6.1, 2H), 3.51 (s, 2H), 2.24 (m, 2H), 1.34 (s, 4H), 1.16 (s, 6H). ^{13}C NMR (101 MHz, methanol-d_4) δ 126.01, 126.72–117.13 (q, $^1J_{C-F}$ = 292.3 Hz), 80.97 (m, $^2J_{C-F}$ = 30.5 Hz), 69.21, 67.12, 67.06, 66.36, 65.84, 58.98, 51.78, 48.46, 47.88, 47.51, 31.31, 18.08, 17.21. ^{19}F NMR (376 MHz, MeOD) δ −71.51. ATR-FTIR: stretching O–H: 3650–3100 cm^{-1}; stretching C–H: 3000–2850 cm^{-1}; stretching C=O: 1727 cm^{-1}; stretching C–F: 1250 cm^{-1}; bending C–F: 700 cm^{-1}.

*Compound **5**.* 3-[(2-Methylpropan-2-yl)oxycarbonylamino]propanoic acid (312 mg; 1.65 mmol), EDC (317 mg; 1.65 mmol), and DMAP (8.4 mg; 0.07 mmol) were put under nitrogen atmosphere for 5 minutes. Then, 4 mL of anhydrous CH_2Cl_2 were added. Separately, compound **FJD$_2$** (176 mg; 0.14 mmol) was dissolved in other 3 mL of anhydrous CH_2Cl_2 and then, transferred, by means of other 3 mL of the solvent, to the reaction mixture. The reaction was run at room temperature, under stirring and nitrogen atmosphere overnight. To control the progress of the reaction a TLC was done using as eluent a mixture of hexane and ethyl acetate (6 : 4). To purify the product, a column chromatography on silica flash was made using the same eluent as those for TLC (rf: 0.3). To remove the excess of 3-[(2-methylpropan-2-yl)oxycarbonylamino]propanoic acid, the purified mixture was dissolved in CH_2Cl_2 and washed twice with a 10% m/v aqueous $NaHCO_3$ solution. The organic phase was dried on Na_2SO_4 and a pale-yellow oil was recovered after the removal of the solvent by rotary evaporation (yield: 75%).

^{1}H NMR (400 MHz, $CDCl_3$) δ 7.73 (s, 1H), 5.27 (s, 2H), 4.43 (t, J = 7.3 Hz, 2H), 4.30–4.10 (m, 12H), 4.05 (s, 6H), 3.48 (t, J = 6.0 Hz, 2H), 3.37 (t, J = 6.1 Hz, 8H), 2.53 (t, J = 6.1 Hz, 8H), 2.26–2.16 (m, 2H), 1.43 (s, 36H), 1.25 (s, 3H), 1.20 (s, 6H). ^{19}F NMR (376 MHz, $CDCl_3$) δ −70.36.

FJD$_2$N. Compound **5** (195 mg; 0.10 mmol) was dissolved in 2 mL of anhydrous CH_2Cl_2, under nitrogen atmosphere. Then trifluoroacetic acid (TFA, 2 mL) was slowly added. The reaction was run till the total conversion of the precursor, confirmed by TLC by using as eluent a mixture of hexane and ethyl acetate (1 : 1). The time required is around 1 hour. The reaction was stopped by drying the compound through rotary evaporation. Then the compound was solubilized in hexafluoro-2-propanol and dried again three times to remove the excess of TFA. Then the compound was solubilized in 250 μL of cold methanol and transferred slowly into a vial containing 5 mL of cold ether: after the precipitation at the bottom of the vial of an immiscible oily phase, the supernatant was removed, and the precipitate was dissolved in water and freeze-dried. The compound was collected as a white hydroscopic amorphous solid (yield: 80%). ^{1}H NMR (400 MHz, MeOD) δ 8.07 (s, 1H), 5.27 (s, 2H), 4.49 (t, J = 7.2 Hz, 2H), 4.34–4.21 (m, 12H), 4.15 (s, 6H), 3.50 (t, J = 6.1 Hz, 2H), 3.45 (s, 2H), 3.23 (t, J = 6.7 Hz, 8H), 2.80 (t, J = 6.7 Hz, 8H), 2.19 (p, J = 6.4 Hz, 2H), 1.29 (s, 3H), 1.24 (s, 6H). ^{13}C NMR (101 MHz, MeOD) δ 173.48, 171.80, 126.23, 121.59 (q, J = 293.1 Hz), 80.50–81.0 (m), 69.24, 67.13, 67.03, 66.93, 66.85, 59.05, 47.98, 47.48, 36.31, 31.32, 17.91, 17.83. ^{19}F NMR (376 MHz, MeOD) δ −71.46, −76.82. ATR-FTIR: stretching N–H: 3600–3350 cm^{-1}; stretching C–H: 3200–2850 cm^{-1}; stretching C=O: 1735 cm^{-1}, 1674 cm^{-1}; stretching C–F: 1230 cm^{-1}; bending C–F: 736 cm^{-1}; HRMS (ESI) for $C_{50}H_{63}N_7O_{18}F_{27}$ – theoretical $[M\text{-}H]^+$: 1562.3798/Found $[M\text{-}H]^+$: 1562.3794, Copper content: 191 ppm by ICP-OES.

pK_a determination. The pK_a was determined by following an already reported procedure.[51] A drop of each solution was analyzed in triplicate by a Pocket ISFET pH Meter Model 24006 whose calibration was performed as reported by the vendor instructions. A solution of **FJD$_2$N** was prepared dissolving 7.73 mg of **FJD$_2$N** in 7 mL of NaCl 1 mM. 2 μL of a NaOH standard solution (0.1 N, Titripur® Reagent from Merck) were added at each point under stirring till pH = 9.8. pH was measured in triplicate at each point (pH used for the graph construction is an average of the three values).

NMR titration for association constant determination. A solution 4.03 mM of **FJD$_2$N** in deuterated DMSO was prepared. A known amount of tetrabutylammonium chloride (TBAC) was dissolved in 1 mL of **FJD$_2$N** solution, thus maintaining the concentration of **FJD$_2$N** constant during all additions. Further additions (10 μL) of TBAC solution to 400 μL of **FJD$_2$N** 4.03 mM were performed. After each TBAC addition ^{1}H-NMR and ^{19}F-NMR analyses were done. The binding constant was calculated using Bindfit with a 1 : 1 *H*/*G* model ratio (http://app.supramolecular.org/bindfit/).[70]

Fluorescence titration for association constant determination. To 20 μL of a 31.25 μM stock solution of double strand Cy5-modified Luciferase GL3 (CUUACGCUGAGUACUUCGA), purchased from Eurofins Genomics, were mixed increasing amount of **FJD$_2$N** at final concentrations reported in Table S5 in SI, in a total final volume of 1 mL of MilliQ water. Fluorescence emission and excitation spectra were recorded with a commercial spectrofluorometer (Jasco, FP-8500) at λ_{ex} = 651 nm and λ_{em} = 654–750 nm. The binding constant was calculated using Bindfit with a 2 : 1 *H*/*G* model ratio (http://app.supramolecular.org/bindfit/).[70]

Evaluation of the oligonucleotides binding ability. The binding ability of **FJD$_2$N** to complex nucleic acids has been determined for both DNA and siRNA sequences in HEPES buffer 10 mM, pH 7.4 or in NaCl 150 mM. Salmon sperm DNA, composed by 2000 base pairs, and Luciferase GL3, double strand siRNA (CUUACGCUGAGUACUUCGA), were used. The N/P ratio was determined monitoring the fluorescence emission of SYBR® green in the presence of a constant amount of the NAs and an increasing amount of **FJD$_2$N**. The binding ability of **FJD$_2$N** was monitored by a fluorophore-displacement assay, as reported elsewhere.[71–73] Briefly, complexes were invariably prepared by mixing 1.0 μL of DNA (0.50 μg μL^{-1} in TE 0.1×) in 1.0 μL of SYBR® Green I (λ_{ex} = 497 nm, λ_{em} = 520 nm) with 11.8 μL of the **FJD$_2$N** solutions at different concentrations. Afterward, complexes were incubated for 20 minutes at room temperature in the dark, then diluted to a final volume of 200 μL in the solvent. Fluorescence measurements (n = 3) were performed with a Synergy H1 spectrophotometer (BioTek, Italy) in 384-multiwell black plates (λ_{ex} = 487 nm, λ_{em} = 528 nm). Data are expressed as relative fluorescence values normalized to the fluorescence of uncomplexed, pristine DNA.

FJD$_2$N self-assembling properties in aqueous solutions

CMC determination in water. The procedure was done by slightly modifying an already reported procedure.[74] A pyrene solution was prepared by dissolving 5 mg in 10 mL of methanol (2.5 mM), then diluted 400 times with Methanol (pyrene: 6.25 μM). To prepare the working mixtures for fluorescence measurements, a small aliquot (17 μL) of the latter pyrene solution was transferred to the solution of **FJD$_2$N** in MilliQ water at the desired concentration till a final volume of 1 mL (pyrene: 100 nM). Fluorescence emission and excitation spectra were obtained with a commercial spectrofluorometer (Jasco, FP-8500).

CMC determination in NaCl 150 mM. To prepare the working mixtures for fluorescence measurements, a small aliquot (17 μL) of the 6.25 μM pyrene solution was transferred to the solution of **FJD$_2$N** in NaCl 150 mM at the desired concentration till a final volume of 1 mL (pyrene: 100 nM). Fluorescence emission and excitation spectra were obtained with a commercial spectrofluorometer (Jasco, FP-8500). Table S7 in SI shows the input parameter used to set the experiments. Tables S8 and S9 in SI shows the concentrations of the **FJD$_2$N** solution tested for the CMC determination in MilliQ water and NaCl 150 mM, respectively.

Sample preparation in MilliQ water. Solutions of **FJD$_2$N** were obtained by directly dispersing the amount of the solid

required to obtain the desired concentrations (2.5 mM and 0.5 mM) in MilliQ water. Milli-Q water (mQw, 18.2 mΩ cm^{-1}) used to prepare the aqueous dispersions was obtained by the purification system provided by Simplicity®. NaCl (purity 99%) was purchased from Sigma Aldrich. The solutions were aged at a constant temperature (25 °C) and analyzed after 1 (t_0) hour from the sample preparation, after 24 hours (t_{24}), and 48 hours (t_{48}) of ageing.

Sample preparation in NaCl 150 mM and dendriplexes. Solutions of **FJD_2N** were obtained by directly dispersing the amount of the solid required to obtain the desired concentrations (2.5 mM and 0.5 mM) in NaCl 150 mM. Milli-Q water (mQw, 18.2 mΩ cm^{-1}) used to prepare the aqueous dispersions was obtained by the purification system provided by Simplicity®. NaCl (purity 99%) was purchased from Sigma Aldrich. The solutions were aged at a constant temperature (25 °C) and analyzed after 1 (t_0) hour from the sample preparation, after 24 hours (t_{24}), and 48 hours (t_{48}) of ageing. In case of dendriplexes **FJD_2N** was mixed with siMAX siRNA control – Luciferase GL3 to reach the desired N/P till a final concentration of **FJD_2N** 0.56 mM.

pH determination. A drop of each solution was analyzed in triplicate by a Pocket ISFET pH Meter Model 24006 whose calibration was performed as reported by the vendor instructions.

Dynamic light scattering measurements. Multiangle DLS was measured at ALV compact goniometer system, equipped with ALV-5000/EPP Correlator, special optical fiber detector and ALV/GCS-3 compact goniometer, with He–Ne laser (λ = 633 nm, 22 mW output power) as light source. The temperature was controlled with a thermostatic bath and set at 25 °C. A volume comprised between 800 μL and 1 mL was used for the analysis. DLS was measured at different time points (0, 24, 48 hours) and scattering angles θ = 70–130° in 20° steps. Each measure was the result of the average of three subsequent run of 10 seconds each, with a threshold sensibility of 10%. Data analysis was done with ALV-Correlator software. The apparent hydrodynamic radii at different angles were obtained from an intensity weighted and a number weighted fitting of the autocorrelation function. Hydrodynamic radii (R_H) and polydispersity indexes (PDI) were calculated using the cumulant fitting. For a more accurate analysis, precluded with cumulant fitting due to the high polydispersity of the samples, CONTIN analyses were performed, and sizes distributions are reported according to intensity and number weighted equations.

Z potential measurements. Z potential was measured at 25 °C in folded capillary cells (U-shaped cells with two gold plated beryllium/copper electrodes at the top) 48 hours later the colloidal dispersion preparation with a Zetasizer Nano ZS (Malvern Instrument, Malvern, Worcestershire, UK), equipped with a 633 nm laser. Before each measure, the cells were cleaned with MilliQ water and then filled up with approximately 1 mL of sample solution, checking that the gold-plated electrodes were immersed and that there were no bubbles inside the cell.

^{19}F-NMR spectra. To perform the ^{19}F-NMR spectra 500 μL of the 2.5 mM and the 0.5 mM **FJD_2N** solutions were mixed with 50 μL of deuterated water, added to perform the lock at the NMR instrument. Spectra were collected by setting 256 number of scans as input parameter. The peak of the TFA anions has been set at −75.45 ppm.

SAXS. The SAXS measurements were performed with a Xeuss 3.0 UHR SAXS/WAXS system (Xenocs SAS, Grenoble, France) equipped with a GeniX 3D Cu K alpha radiation source ($\lambda \approx$ 1.54 Å) and with in-vacuum motorized 3-axis Q-Xoom Eiger2 R 1M detector (Dectris Ltd, Switzerland) for 2D SAXS/WAXS data collection. The configuration chosen for the measurements covered a q range of 0.007 < q (Å^{-1}) < 0.5 Å^{-1}, where $q = 4\pi/\lambda \sin(\theta/2)$, q is the modulus of the scattering vector, λ the wavelength, and θ the scattering angle. The samples were measured in quartz capillary of 1.5 mm diameter at RT and under vacuum (<0.09 mbar). The concentration of the samples for these measurements was 0.56 mM of **FJD_2N**. The sample was measured at two sample-detector distances of 350 mm and 900 mm for 30 min and 90 min, respectively. The 2D SAXS patterns were radially integrated into the one-dimensional scattering intensity $I(q)$ and merged. The data presented are background subtracted using the macros in Igor Pro,[75] where the background corresponds to the solvent measured in an analogue capillary. The SAXS intensities are represented in absolute units.

SANS. The SANS data were collected on the ZOOM diffractometer at the ISIS Neutron and Muon Source (Rutherford Appleton Laboratory, Science and Technology Facilities Council, UK). Data were collected in the q-range 0.0025–0.45 Å^{-1} using a sample-to-detector distance and collimation length of 8 m, and wavelengths in the range 1.75–15 Å. The concentration of **FJD_2N** in the samples for these measurements was 0.5 and 2.5 mM. Samples were loaded in quartz cells (1 mm pathlength) and then placed in a temperature-controlled sample changer, and temperature was set to 25 °C. The acquisition time was 1 to 2 hours from preparation depending on sample concentration and solvent contrast. SANS curves were collected for all solvent contrasts in the same conditions as the samples and used as background. Raw data were radially averaged, corrected for detector efficiency, scaled for absolute intensity and background subtracted according to standard procedures in Mantid software.[61] All the data were merged and background subtracted using the macro on Igor Pro.[75]

Cryo-TEM. Dispersions analyzed: **FJD_2N** alone (0.56 mM), dendriplexes of **FJD_2N** (0.56 mM) + siRNA control – Luciferase GL3 (N/P = 20), dendriplexes of **FJD_2N** (0.56 mM) + siRNA control – Luciferase GL3 (N/P = 30), and dendriplexes of **FJD_2N** (0.56 mM) + siRNA control – Luciferase GL3 (N/P = 40). Sample vitrification was carried out with a Mark IV Vitrobot (Thermo Fisher Scientific). 4 μL of each dispersion were applied to a Quantifoil R2/1 Cu 300-mesh grid previously glow-discharged at 30 mA for 30″ in a GloQube (Quorum Technologies). Immediately after sample application, the grids were blotted in a chamber at 4 °C and 100% humidity, and then plunge-frozen into liquid ethane.

Vitrified grids were transferred to a Talos Arctica (Thermo Fisher Scientific) operated at 200 kV and equipped with a

Falcon 3 direct electron detector (Thermo Fisher Scientific). Micrographs were acquired in linear mode, with a defocus of −3.0 μm and with a total dose of 40 e^{-} $Å^{-2}$.

T_1 and T_2 experiments by ^{19}F-NMR and ^{19}F-MRI phantom experiments. T_1 and T_2 measurements were obtained on the **FJD$_2$N** solution 2.5 mM in MilliQ water and on the **FJD$_2$N** solution 0.56 mM in NaCl 150 mM. The fitting of the data was performed by a single exponential fit and raw data were analyzed by the Bruker TopSpin software and MestReNova software.

^{19}F-MRI acquisitions were performed immediately after dispersing **FJD$_2$N** samples in pure water (MQW), NaCl 150 mM, and in presence of siRNA Luciferase GL3 (N/P = 30) at three different concentrations ranging from 0.5 to 2.5 mM. Samples containing control vehicle (MQW) was recorded to determine the noise threshold. Each sample was loaded into a 0.2 mL Eppendorf tubes and positioned within a phantom containing 2% agar gel. All experiments were conducted on a 7T scanner (Biospec; Bruker-Biospin) using a dual-transmit receive ^{19}F/^{1}H volume coil (35 × 59 mm) integrated with an ultra-shielded horizontal bore magnet. ^{19}F-MR images were obtained at the specific resonance frequency of **FJD$_2$N** (−71.3 ppm). A 3D turbo-spin echo sequence was employed for all imaging acquisitions, maintaining the same field of view (45 × 30 × 24 mm) for both ^{1}H-MRI (TR/TE = 250/15 ms, matrix = 128 × 64 × 8, 6 averages) and ^{19}F-MRI (TR/TE = 1500/40 ms, matrix = 64 × 32 × 8, 32 averages). For each sample, the signal-to-noise ratio (SNR) was quantified using the image analysis software of the scanner (Paravision 6.0, Bruker Biospin). Specifically, the mean signal intensity within the sample area on the ^{19}F image was calculated and divided by the standard deviation of the noise measured in three different background regions of the image outside the sample. As shown in Fig. S16, the SNR of **FJD$_2$N** was detectable only at a concentration of 2.5 mM for all conditions.

Cytotoxicity and transfection efficacy on different cell lines

L929 (murine fibroblast from subcutaneous connective tissue, ATCC®-CCL-1™), SH-5YSY (human neuroblastoma, ATCC® CRL-2266™) and C2C12 (murine myoblasts, ATCC® CRL-1772™) cell lines were purchased from the American Type Culture Collection (ATCC, Manassas, VA, USA). AlamarBlue Cell Viability Assay was from Life Technologies Italia (Monza, Italy), while BCA Protein Assay Kit was from ThermoFisher (Monza, Italy). pDNA encoding the secreted Luciferase from the copepod Gaussia princeps (pGLuc-Basic 2 (pGLuc), 4.958 kbp) and BioLux® Gaussia Luciferase Assay Kit were obtained from New England Biolabs Inc. (Ipswich, MA, USA). siMAX siRNA control Luciferase GL3 was purchased from Eurofins Genomics.

Preparation of transfectant solution. **FJD$_2$N** was diluted in NaCl 150 mM or HEPES buffer 10 mM to a final concentration of 2.5 mM, corresponding to a final concentration of positive charges [N] = [+] = 10 mM, if a 100% protonation is considered.

L929 were cultured in Dulbecco's modified Eagle's medium (DMEM) containing 1 mM sodium pyruvate, 10 mM HEPES buffer, 100 U mL^{-1} penicillin, 0.1 mg mL^{-1} streptomycin, 2 mM glutamine and supplemented with 10% v/v fetal bovine serum (FBS) in a humidified atmosphere under constant supply of 5% v/v CO_2 and at 37 °C (hereinafter referred as to standard culture condition). SH-5YSY cells were cultured in 40% v/v Eagle's Minimum Essential Medium (EMEM), 40% v/v F12 medium, 1% v/v NEAA, 100 U mL^{-1} penicillin, 0.1 mg mL^{-1} streptomycin, 2 mM glutamine and supplemented with 15% v/v FBS in a standard culture condition. C2C12 cells were cultured in DMEM containing 1% v/v L-glutamine, 1% v/v Pen/Strep, 1% v/v insulin, 10 ng μL^{-1} EGF, 10 ng μL^{-1} β-FGF and supplemented with 10% v/v FBS in a standard culture condition.

Twenty-four hours before transfection, cells were seeded onto 96-well plates at a density of 2×10^4 cells per cm^2 and maintained in standard culture conditions.

Next, 100 ng per well of pGLuc were complexed in NaCl 150 mM with **FJD$_2$N** solutions to yield different N/P ratios, as described in Table S17 in SI, jetPEI®, according to the protocol,[67] or Lipofectamine™ 3000, and cells were incubated with complexes in 100 μL per well of cell culture medium under standard culture conditions for 24 hours.

Following a 24 hour transfection, cytotoxicity was evaluated using AlamarBlue assay according to manufacturer's instructions. Briefly, the medium was discarded, and each well was filled with 100 μL of 1× resazurin dye-containing culture medium. Cells were next incubated in standard culture conditions for 2 hours, then the fluorescence of the medium was read with a Synergy H1 spectrophotometer (BioTek, Italy) (λ_{ex} = 540 nm; λ_{em} = 595 nm). Viability of untransfected cells (CTRL) was assigned to 100% and cytotoxicity was calculated as follows:

$$\text{Cytotoxicity}\,(\%) = 1 - \left[\frac{\text{RFU}_{\text{transfected cells}}}{\text{RFU}_{\text{CTRL}}}\right] \times 100.$$

Transfection efficiency was evaluated by measuring the luciferase activity by means of the Luciferase Assay System, according to manufacturer's instructions. Briefly, from each well, 10 μL of supernatant were added to 50 μL of Luciferase Assay Reagent and luminescence was measured using a Synergy H1 spectrophotometer. Transfection efficiencies were expressed as luminescence signal (expressed as relative light units, RLU) of each sample.

***In vitro* viability and internalization assessment through confocal microscopy.** Gibco™ Trypan Blue was purchased from Thermo Fisher Scientific. siMAX siRNA control Cy5-modified Luciferase GL3 was purchased from Eurofins Genomics.

C2C12 cells were cultured in proliferative medium and then, 24 hours before the treatment, seeded with a density of 3×10^4 cells per well in a 24-well multiwell. Next, the cells were treated with nanoparticles (NP) 30-bound siRNA Cy5-modified Luciferase GL3 and with **FJD$_2$N** alone and cultured for 24, 48 and 72 hours. For each time point cells were collected for Trypan Blue exclusion assays[76] and immunofluorescence analyses.

Cell viability was assessed by resuspending the cell pellet in 1 mL of culture medium and mixing 10 μL of resuspended cells with 10 μL of Trypan. Next, 10 μL of the obtained solution was inserted into a Burker counting chamber and checked through optical microscopy (Eclipse TE 2000-S, Nikon, Tokyo, Japan).

For the immunostaining, C2C12 cells were fixed in 4% paraformaldehyde at room temperature for 20 min, permeabilized with 0.1% Triton X-100, and treated with 5% normal goat serum in PBS to block non-specific binding. Next, they were incubated with rabbit anti-desmin primary antibodies. Secondary antibodies were Alexa Fluor 488-conjugated goat anti-rabbit IgG. Myoblasts were counterstained with DAPI and the coverslips were mounted with FluorSave. Confocal fluorescence images were obtained with a laser-scanning microscope (Eclipse TE 2000-E, Nikon) and analyzed using EZ-C1 3.70 imaging software (Nikon). The variation in Cy5-siRNA fluorescence intensity over time was evaluated using the Corrected Total Cell Fluorescence (CTCF) method.[77] Images elaboration was performed using Fiji ImageJ software.[78]

Conclusions

We developed a simple and scalable Janus-type amphiphilic dendrimer, **FJD$_2$N**, including a multi-branched fluorinated moiety as the hydrophobic part. The optimal balance and dimensions of its hydrophobic and hydrophilic domains enable the dendrimer to self-assemble into stable micellar dispersions in water, eliminating the need for any additional formulation components. The primary ammonium groups within the hydrophilic region facilitate efficient multivalent coordination of anions, ensuring excellent binding affinity. As a result, **FJD$_2$N** demonstrates effective NA carrier capabilities, achieving high NA internalization across various cell lines, while maintaining low cytotoxicity, despite its positive charge in physiological conditions. Moreover, preliminary ^{19}F-MRI phantom experiments confirmed the possibility to visualize **FJD$_2$N** dendriplexes. Future studies are needed to better understand the mechanism of cells internalization and biological effectiveness. However, our findings already demonstrated that **FJD$_2$N** is an efficient, safe, and ^{19}F-MRI traceable non-viral vector to deliver NAs into cells.

Author contributions

P. M. and F. B. B. designed the project, secured funding, supervised project realization, and share corresponding authorship; M. R., L. F., and B. L. B. performed dendrimer synthesis and physico-chemical characterization; N. B. and L. F. performed *in vitro* cell studies on L929, SH-SY5Y, C2C12. N. B. and G. Candiani designed *in vitro* gene delivery studies; F. S., F. B. B. and N. M. performed SANS experiments, analyses, data processing, and interpretation; G. R. performed AAMD simulations; G. Cavallo supervised dendrimer synthesis; L. F., N. I., and C. M. performed *in vitro* cells studies on C2C12; S. M. and G. L. supervised biological tests; A. C.-S. performed Cryo-TEM experiments. All authors contributed to article writing and revising, M. R., P. M., and F. B. B. in particular, and approved it for publication.

Conflicts of interest

The authors declare no conflict of interest.

Abbreviations

AAMD	All-atom molecular dynamics
ALS	Amyotrophic lateral sclerosis
ATR-FTIR	Attenuated total reflection-Fourier transform infrared spectroscopy
Bis-MPA	2,2-Bis(hydroxymethyl)propionic acid
Boc	Tert-butyloxycarbonyl protecting group
CMC	Critical micelle concentration
Cryo-TEM	Cryogenic transmission electron microscopy
CTCF	Corrected total cell fluorescence
CTRL	Control
DAPI	4′,6-Diamidino-2-phenylindole
DLS	Dynamic light scattering
DMSO	Dimethyl sulfoxide
EDTA	Ethylenediaminetetraacetic acid disodium salt
FJD$_{1-3}$	Non-ionic fluorinated bis-MPA Janus dendrimers (generations 1–3)
FJD$_1$N	Protonable fluorinated Janus dendrimer of 1st generation
FJD$_2$N	Protonable fluorinated Janus dendrimer of 2nd generation
HB	Hydrogen bonding
HEPES	(4-(2-Hydroxyethyl)-1-piperazineethanesulfonic acid)
HRMS	High resolution mass spectrometry
ICP-OES	Inductively coupled plasma optical emission spectroscopy
LNP	Lipid nanoparticles
MD	Molecular dynamics
N/P	Nitrogen to phosphorus ratio
NA	Nuclei acids
NMR	Nuclear magnetic resonance
NVT	Number of particles, volume, and temperature is constant
p.p.	Packing parameter
PAMAM	Polyamidoamine
PDI	Polydispersity index
RT	Room temperature
SANS	Small-angle neutron scattering
SAXS	Small-angle X-ray scattering
SD	Standard deviation
SE	Standard error

SLD	Scattering length density
TBAC	Tetrabutylammonium chloride
TFA	Trifluoroacetic acid
THF	*Tetrahydrofuran*
TLC	Thin layer chromatography.

Data availability

The data supporting this article have been included as part of the supplementary information (SI). Supplementary information: additional experimental details, tables, and figures as mentioned in the text. See DOI: https://doi.org/10.1039/d5nr03209a.

Acknowledgements

This work was supported by the Italian Ministry of Health (RRC); Fondazione Regionale per la Ricerca Biomedica (FRRB); TRANS-ALS, Grant No. 2015-0023; CALabria HUB per Ricerca Innovativa ed Avanzata – CALHUB.RIA "Creazione di Hub delle Scienze della Vita" T4-AN-09 prog. ZRPOS2. M. R., F. B. B., and P. M. also acknowledge the INNOVA project (funded by Ministero della Salute, PNC-E3-2022-23683266). F. B. B. acknowledges the project Lancelot (PRIN 2022 PNRR nP2022RBF5P) funded by MUR (European Union – NextGeneration EU). The Small Angle X-ray Scattering experiments were carried out at the Next-GAME Laboratory of the Politecnico di Milano, co-funded by Regione Lombardia. The cryo-EM experiments were carried out at the NoLimits center of the University of Milan. We thank Tamara Canu and Antonio Esposito, MD, PhD (Center of Experimental Imaging, CIS, IRCCS San Raffaele Hospital), for access to the 7-T MRI facility. The authors thank the ISIS Neutron and Muon Source (STFC, Didcot, UK) for allocation of beam time on ZOOM with a corresponding number: https://doi.org/10.5286/ISIS.E.RB2310070. This work benefited from the use of the SasView application, originally developed under NSF award DMR-0520547. SasView contains code developed with funding from the European Union's Horizon 2020 research and innovation program under the SINE2020 project, grant agreement no. 654000.

References

1 C. Chen, W. Law, C. Chu, N. Chen and L. Lo, *Int. J. Nanomed.*, 2020, **15**, 2131–2150.
2 R. Bholakant, H. Qian, J. Zhang, X. Huang, D. Huang, J. Feijen, Y. Zhong and W. Chen, *Biomacromolecules*, 2020, **21**, 2966–2982.
3 H. V. Balcorta, V. G. Contreras Guerrero, D. Bisht and W. Poon, *ACS Appl. Bio. Mater.*, 2024, **7**, 5020–5036.
4 Q. Wang, C. Bu, Q. Dai, J. Chen, R. Zhang, X. Zheng, H. Ren, X. Xin and X. Li, *Adv. Sci.*, 2024, **11**, 2309748.
5 J. Schock Vaiani, M. Broekgaarden, J. L. Coll, L. Sancey and B. Busser, *Nanoscale*, 2025, **17**, 5501–5525.
6 C. C. Lim, L. Y. Chia and P. V. Kumar, *OpenNano*, 2023, **13**, 100173.
7 P. Stenström, D. Manzanares, Y. Zhang, V. Ceña and M. Malkoch, *Molecules*, 2018, **23**, 2028.
8 J. H. Bae, H. S. Kim, G. Kim, J. J. Song and H. S. Kim, *Adv. Sci.*, 2021, **8**, 2102991.
9 S. Svenson, *Chem. Soc. Rev.*, 2015, **44**, 4131–4144.
10 D. A. Tomalia, *Pharmaceutics*, 2024, **16**, 403.
11 A. Barnard, P. Posocco, S. Pricl, M. Calderon, R. Haag, M. E. Hwang, V. W. T. Shum, D. W. Pack and D. K. Smith, *J. Am. Chem. Soc.*, 2011, **133**, 20288–20300.
12 Y. G. Gao, X. Lin, K. Dang, S. F. Jiang, Y. Tian, F. L. Liu, D. J. Li, Y. Li, Z. P. Miao and A. R. Qian, *Org. Biomol. Chem.*, 2018, **16**, 7833–7842.
13 T. Yu, X. Liu, A. L. Bolcato-Bellemin, Y. Wang, C. Liu, P. Erbacher, F. Qu, P. Rocchi, J. P. Behr and L. Peng, *Angew. Chem., Int. Ed.*, 2012, **51**, 8478–8484.
14 S. Malhotra, H. Bauer, A. Tschiche, A. M. Staedtler, A. Mohr, M. Calderón, V. S. Parmar, L. Hoeke, S. Sharbati, R. Einspanier and R. Haag, *Biomacromolecules*, 2012, **13**, 3087–3098.
15 D. Zhang, E. N. Atochina-Vasserman, D. S. Maurya, M. Liu, Q. Xiao, J. Lu, G. Lauri, N. Ona, E. K. Reagan, H. Ni, D. Weissman and V. Percec, *J. Am. Chem. Soc.*, 2021, **143**, 17975–17982.
16 Q. Laurent, B. L. Bona, J. Asohan, M. Rosati, S. Faiad, F. Baldelli Bombelli, P. Metrangolo and H. F. Sleiman, *Angew. Chem., Int. Ed.*, 2025, **64**, e202419996.
17 J. Liu, C. Chen, T. Wei, O. Gayet, C. Loncle, L. Borge, N. Dusetti, X. Ma, D. Marson, E. Laurini, S. Pricl, Z. Gu, J. Iovanna, L. Peng and X. J. Liang, *Exploration*, 2021, **1**, 21–34.
18 G. Chen, Y. Wang, A. Ullah, Y. Huai and Y. Xu, *Eur. J. Pharm. Sci.*, 2020, **152**, 105433–105440.
19 D. Sahoo, M. Peterca, M. R. Imam, D. S. Maurya and V. Percec, *J. Mater. Chem. B*, 2024, **12**, 12265.
20 S. Wang, J. Xing, B. Xiong, H. Han, M. Hu and Q. Li, *Macromol. Biosci.*, 2021, 2100024–2100032.
21 J. Lv, H. Wang, G. Rong and Y. Cheng, *Acc. Chem. Res.*, 2022, **55**, 722–733.
22 Y. Qi, H. Song, H. Xiao, G. Cheng, B. Yu and F. J. Xu, *Small*, 2018, **14**, 1803061.
23 S. Wang, J. Xing, B. Xiong, H. Han, M. Hu and Q. Li, *Macromol. Biosci.*, 2021, **21**, 1–8.
24 P. Zhang, R. Guo, H. Zhang, W. Yang and Y. Tian, *Adv. Sci.*, 2023, **10**, 2304633.
25 A. Vasukutty, S. Chahal, K. Lee, S. Park, S. Kim, E. Shin, Y. Kim, D. Kim, J. Lee, H. Jeong and I. Park, *Adv. Healthc. Mater.*, 2024, **14**, 2403374.
26 C. Chirizzi, C. Morasso, A. A. Caldarone, M. Tommasini, F. Corsi, L. Chaabane, R. Vanna, F. B. Bombelli and P. Metrangolo, *J. Am. Chem. Soc.*, 2021, **143**, 12253–12260.
27 I. Tirotta, A. Mastropietro, C. Cordiglieri, L. Gazzera, F. Baggi, G. Baselli, M. Grazia Bruzzone, I. Zucca,

G. Cavallo, G. Terraneo, F. Baldelli Bombelli, P. Metrangolo and G. Resnati, *J. Am. Chem. Soc.*, 2014, **136**, 8524–8527.
28 M. Wang, H. Liu, L. Li and Y. Cheng, *Nat. Commun.*, 2014, **5**, 3053.
29 C. Romani, P. Gagni, M. Sponchioni and A. Volonterio, *Bioconjugate Chem.*, 2023, **34**, 1084–1095.
30 M. Wang and Y. Cheng, *Acta Biomater.*, 2016, **46**, 204–210.
31 X. Liu, Y. Yuan, S. Bo, Y. Li, Z. Yang, X. Zhou, S. Chen and Z. X. Jiang, *Eur. J. Org. Chem.*, 2017, **2017**, 4461–4468.
32 V. Dichiarante, I. Tirotta, L. Catalano, G. Terraneo, G. Raffaini, M. R. Chierotti, R. Gobetto, F. Baldelli Bombelli and P. Metrangolo, *Chem. Commun.*, 2017, **53**, 621.
33 G. Tedeschi, S. Guzman-Puyol, L. Ceseracciu, J. J. Benitez, L. Goldoni, A. Koschella, T. Heinze, G. Cavallo, V. Dichiarante, G. Terraneo, A. Athanassiou, P. Metrangolo and J. A. Heredia-Guerrero, *Carbohydr. Polym.*, 2021, **271**, 118031.
34 A. K. Singh, B. Schade, M. Rosati, R. Rashmi, V. Dichiarante, G. Cavallo, P. Metrangolo and R. Haag, *Macromol. Biosci.*, 2022, **22**, 2200108.
35 T. Guitton-Spassky, B. Schade, C. Zoister, E. Veronese, M. Rosati, F. Baldelli Bombelli, G. Cavallo, A. F. Thünemann, H. Ghermezcheshme, H. Makki, R. R. Netz, K. Ludwig, P. Metrangolo, A. K. Singh and R. Haag, *JACS Au*, 2025, **5**, 2223–2236.
36 G. Cavallo, G. Terraneo, A. Monfredini, M. Saccone, A. Priimagi, T. Pilati, G. Resnati, P. Metrangolo and D. W. Bruce, *Angew. Chem., Int. Ed.*, 2016, **55**, 6300–6304.
37 M. Wang and Y. Cheng, *Acta Biomater.*, 2016, **46**, 204–210.
38 X. Liu, Y. Wang, C. Chen, A. Tintaru, Y. Cao, J. Liu, F. Ziarelli, J. Tang, H. Guo, R. Rosas, S. Giorgio, L. Charles, P. Rocchi and L. Peng, *Adv. Funct. Mater.*, 2016, **26**, 8594–8603.
39 J. Liu, C. Chen, T. Wei, O. Gayet, C. Loncle, L. Borge, N. Dusetti, X. Ma, D. Marson, E. Laurini, S. Pricl, Z. Gu, J. Iovanna, L. Peng and X. J. Liang, *Exploration*, 2021, **1**, 21–34.
40 Z. Lyu, B. Ralahy, T. A. Perles-Barbacaru, L. Ding, Y. Jiang, B. Lian, T. Roussel, X. Liu, C. Galanakou, E. Laurini, A. Tintaru, S. Giorgio, S. Pricl, X. Liu, M. Bernard, J. Iovanna, A. Viola and L. Peng, *Proc. Natl. Acad. Sci. U. S. A.*, 2024, **121**, e2322403121.
41 H. Liu, Y. Wang, M. Wang, J. Xiao and Y. Cheng, *Biomaterials*, 2014, **35**, 5407–5413.
42 X. Cai, R. Jin, J. Wang, D. Yue, Q. Jiang, Y. Wu and Z. Gu, *ACS Appl. Mater. Interfaces*, 2016, **8**, 5821–5832.
43 X. Cai, H. Zhu, Y. Zhang and Z. Gu, *ACS Appl. Mater. Interfaces*, 2017, **9**, 9402–9415.
44 J. Movellan, R. González-Pastor, P. Martín-Duque, T. Sierra, J. M. De La Fuente and J. L. Serrano, *Macromol. Biosci.*, 2015, **15**, 657–667.
45 M. Rosati, A. Acocella, A. Pizzi, G. Turtù, G. Neri, N. Demitri, Nonappa, G. Raffaini, B. Donnio, F. Zerbetto, F. B. Bombelli, G. Cavallo and P. Metrangolo, *Macromolecules*, 2022, **55**, 2486–2496.
46 C. Chen, P. Posocco, X. Liu, Q. Cheng, E. Laurini, J. Zhou, C. Liu, Y. Wang, J. Tang, V. D. Col, T. Yu, S. Giorgio, M. Fermeglia, F. Qu, Z. Liang, J. J. Rossi, M. Liu, P. Rocchi, S. Pricl and L. Peng, *Small*, 2016, **12**, 3667–3676.
47 S. Stefanovic, K. McCormick, S. Fattah, R. Brannigan, S. A. Cryan and A. Heise, *Polym. Chem.*, 2023, **14**, 3151–3159.
48 J. Hu, T. Xu and Y. Cheng, *Chem. Rev.*, 2012, **112**, 3856–3891.
49 C. Ma, D. Zhu, W. Lin, Y. Li, Y. Huang, H. Zhu, M. Ye, Y. Wang, L. Peng and X. Liu, *Chem. Commun.*, 2022, **58**, 4168–4171.
50 M. Ramanathan, L. K. Shrestha, T. Mori, Q Ji, J. P. Hill and K. Ariga, *Phys. Chem. Chem. Phys.*, 2013, **15**, 10580–10611.
51 A. Chen, A. Karanastasis, K. R. Casey, M. Necelis, B. R. Carone, G. A. Caputo and E. F. Palermo, *ACS Appl. Mater. Interfaces*, 2020, **12**, 21270–21282.
52 C. Bazzicalupi, A. Bianchi, C. Giorgi, P. Gratteri, P. Mariani and B. Valtancoli, *Dalton Trans.*, 2013, **42**, 12130–12138.
53 V. S. Trubetskoy, P. M. Slattum, J. E. Hagstrom, J. A. Wolff and V. G. Budker, *Anal. Biochem.*, 1999, **267**, 309–313.
54 E. Froehlich, J. S. Mandeville, C. M. Weinert, L. Kreplak and H. A. Tajmir-Riahi, *Biomacromolecules*, 2011, **12**, 511–517.
55 J. Sobek and R. Schlapbach, *Molecules*, 2020, **25**, 5369.
56 H. Wang, S. Ding, Z. Zhang, L. Wang and Y. You, *J. Gene Med.*, 2019, **21**, e3101.
57 A. Tschiche, A. M. Staedtler, S. Malhotra, H. Bauer, C. Böttcher, S. Sharbati, M. Calderón, M. Koch, T. M. Zollner, A. Barnard, D. K. Smith, R. Einspanier, N. Schmidt and R. Haag, *J. Mater. Chem. B*, 2014, **2**, 2153–2167.
58 J. Stetefeld, S. A. McKenna and T. R. Patel, *Biophys. Rev.*, 2016, **8**, 409–427.
59 J. Teixema, *Small-Angle Scattering by Fractal Systems*, 1988, vol. 21.
60 R. Amal, J. A. Raper and T. D. Waite, *Fractal Structure of Hematite Aggregates*, 1990.
61 O. Arnold, J. C. Bilheux, J. M. Borreguero, A. Buts, S. I. Campbell, L. Chapon, M. Doucet, N. Draper, R. Ferraz Leal, M. A. Gigg, V. E. Lynch, A. Markvardsen, D. J. Mikkelson, R. L. Mikkelson, R. Miller, K. Palmen, P. Parker, G. Passos, T. G. Perring, P. F. Peterson, S. Ren, M. A. Reuter, A. T. Savici, J. W. Taylor, R. J. Taylor, R. Tolchenov, W. Zhou and J. Zikovsky, *Nucl. Instrum. Methods Phys. Res., Sect. A*, 2014, **764**, 156–166.
62 X. Wang, J. Chen, D. Wang, S. Dong, J. Hao and H. Hoffmann, *Adv. Colloid Interface Sci.*, 2017, **246**, 153–164.
63 D. Jirak, A. Galisova, K. Kolouchova, D. Babuka and M. Hruby, *Magn. Reson. Mater. Phys., Biol. Med.*, 2019, **32**, 173–185.
64 C. Zhang, S. S. Moonshi, Y. Han, S. Puttick, H. Peng, B. J. A. Magoling, J. C. Reid, S. Bernardi, D. J. Searles, P. Král and A. K. Whittaker, *Macromolecules*, 2017, **50**, 5953–5963.

65 C. A. Terry, M. J. Fernández, L. Gude, A. Lorente and K. B. Grant, *Biochemistry*, 2011, **50**, 10375–10389.
66 H. Ali-Jerman, Z. Al-Quraishi, A. Muglikar, Y. Perrie, R. J. Tate, M. Mullin, G. McNeill, G. Mackenzie and C. Dufès, *Int. J. Nanomed.*, 2024, **19**, 12189–12203.
67 Polyplus, 2013, 5–6.T.
68 T. Wang, L. M. Larcher, L. Ma and R. N. Veedu, *Molecules*, 2018, **23**, 2564.
69 A. Manfredi, N. Mauro, A. Terenzi, J. Alongi, F. Lazzari, F. Ganazzoli, G. Raffaini, E. Ranucci and P. Ferruti, *ACS Macro Lett.*, 2017, **6**, 987–991.
70 D. Brynn Hibbert and P. Thordarson, *Chem. Commun.*, 2016, **52**, 12792–12805.
71 C. Malloggi, D. Pezzoli, L. Magagnin, L. De Nardo, D. Mantovani, E. Tallarita and G. Candiani, *Polym. Chem.*, 2015, **6**, 6325–6339.
72 N. Bono, F. Ponti, D. Mantovani and G. Candiani, *Pharmaceutics*, 2020, **12**, 183.
73 K. Nakanishi, T. Nakasa, N. Tanaka, M. Ishikawa, K. Yamada, K. Yamasaki, N. Kamei, B. Izumi, N. Adachi, S. Miyaki, H. Asahara and M. Ochi, *Spinal Cord*, 2010, **48**, 192–196.
74 A. Domínguez, A. Fernández, N. Gonzalez, E. Iglesias and L. Montenegro, *J. Chem. Educ.*, 1997, **74**, 1227–1231.
75 S. R. Kline, *J. Appl. Crystallogr.*, 2006, **39**, 895–900.
76 W. Strober, *Curr. Protoc. Immunol.*, 2015, **111**, A3.B.1–A3.B.3.
77 O. Gavet and J. Pines, *Dev. Cell*, 2010, **18**, 533–543.
78 J. Schindelin, I. Arganda-Carreras, E. Frise, V. Kaynig, M. Longair, T. Pietzsch, S. Preibisch, C. Rueden, S. Saalfeld, B. Schmid, J. Y. Tinevez, D. J. White, V. Hartenstein, K. Eliceiri, P. Tomancak and A. Cardona, *Nat. Methods*, 2012, **9**, 676–682.